Alkali-wall interactions in a laboratory-scale reactor for chemical looping combustion studies

Fuel Processing Technology 217 (2021) 106828

Contents lists available at ScienceDirect

Fuel Processing Technology

journal homepage: www.elsevier.com/locate/fuproc

Research article

Alkali-wall interactions in a laboratory-scale reactor for chemical looping combustion studies

Viktor Andersson [a], Amir H. Soleimanisalim [b], Xiangrui Kong [a], Fredrik Hildor [c], Henrik Leion [c], Tobias Mattisson [b], Jan B.C. Pettersson [a,*]

[a] Department of Chemistry and Molecular Biology, University of Gothenburg, Sweden
[b] Department of Space, Earth and Environment, Chalmers University of Technology, Sweden
[c] Department of Energy and Materials, Chalmers University of Technology, Sweden

ARTICLE INFO

Keywords:
Laboratory-scale reactor
Alkali
Chemical looping combustion
Surface ionization detector
High temperature corrosion

ABSTRACT

Alkali metal-containing compounds are readily released during thermal conversion of solid fuels, and may have both detrimental and beneficial effects on chemical looping combustion. Here, we characterize alkali interactions with the inner walls of a laboratory-scale reactor under oxidizing, reducing and inert conditions at temperatures up to 900 °C. KCl aerosol particles are continuously introduced to the stainless steel reactor and the alkali concentration is measured on-line with a surface ionization detector. Aerosol particles evaporate at temperatures above 500 °C and KCl molecules rapidly diffuse to the reactor wall. Up to 92% of the alkali reaching the wall below 700 °C remains adsorbed, while re-evaporation is important at higher temperatures, where up to 74% remains adsorbed. Transient changes in alkali concentration are observed during repeated redox cycles, which are associated with changes in chemical composition of the wall material. Metal oxides on the reactor wall are partially depleted under reducing conditions, which allow for the formation of a new potassium-rich phase that is stable in a reducing atmosphere, but not under inert conditions. The observed wall effects are concluded to be extensive and include major transient effects depending on gas composition, and the implications for laboratory studies and improved experimental methodology are discussed.

1. Introduction

Extensive emissions of carbon dioxide from combustion of fossil fuels contribute to climate change and constitute a major threat to society and the environment [1]. One way to reduce emissions is to combine combustion with a system for carbon capture and storage (CCS) [2–4]. This methodology becomes particularly interesting if the fossil fuel is replaced by a biofuel, since it may potentially produce negative CO_2 emissions and reduce atmospheric concentrations on a global scale [2,3]. Chemical-looping combustion (CLC) is one promising technology for CO_2 separation during the combustion of a variety of fuels including solid biomass, and the technology is often superior to other alternatives with regard to the cost of carbon capture [5]. Other advanced biomass conversion technologies under development are based on gasification [6–8] and oxygen carrier aided combustion (OCAC) [9].

Replacing fossil fuels with biofuels is, however, not without challenges. Compared to solid fossil fuels, biomass in general has a higher water content, a lower heating value and produces complex ashes [10]. Biofuels contain relatively high concentrations of potassium and sodium, and alkali metal-containing compounds are readily released during heating. The alkali content is typically around 1 g kg^{-1} in dry stem wood, 4–5 g kg^{-1} in dry wood char and 11 g kg^{-1} in dry straw pellets [11]. During combustion and gasification of biofuels, alkali is known to form deposits that result in agglomeration and corrosion of process equipment such as catalysts, filters and coolers. However, alkali is also known to have some advantages including catalytic effects that may improve fuel conversion [7,12]. Problems that may arise in CLC and OCAC systems are agglomeration of fluidized bed material and associated defluidization [13,14], interaction with oxygen carriers [15,16] and fouling and corrosion of heat exchanger surfaces [10,13]. The alkali species are released during the devolatilization and char burnout stages of biomass conversion [11,12]. The fuel may also contain other components including chlorine, which react with alkali to form volatile alkali chlorides (primarily KCl) that further aggravate problems [12,17].

The unique properties of alkali compounds also affect our ability to carry out detailed studies of their behavior in CLC and other thermal

* Corresponding author.
E-mail address: janp@chem.gu.se (J.B.C. Pettersson).

https://doi.org/10.1016/j.fuproc.2021.106828
Received 30 December 2020; Received in revised form 4 March 2021; Accepted 18 March 2021
Available online 4 April 2021

conversion systems. Several biomass conversion studies have been investigating gaseous alkali components [7,8,11] and alkali interactions with bed materials to study agglomeration [14–16], reactivity [18] and oxygen carrying ablilities [19]. Research has been conducted on both small [20,21] and larger laboratory scales [22–24], small [11,25,26] and larger [27] pilot scales and industrial scale systems [7,8]. Investigations in pilot- or industrial-scale facilities often rely on extractive sampling and chemical transformations and condensation on existing surfaces need to be carefully considered.

Laboratory-scale reactors complement larger facilities and are commonly used for systematic studies of CLC and other thermal conversion processes. Although very valuable for the fundamental understanding of investigated processes, the smaller scale may cause problems that need to be considered when interpreting the results. In general, the surface-to-volume ratio is higher for a laboratory reactor compared to a larger-scale facility. Wall temperatures may also be higher in a small reactor due to external heating, compared to heating caused by an ongoing thermal conversion process at larger scale. The interaction between alkali components and these high temperature surfaces may affect the gas composition in a reactor and thereby interfere with the underlying and specific reactions of interest for the technology, e.g. CLC. In CLC and other related technologies, oxygen carriers are used to transfer oxygen between air and fuel. Thus it is of importance to study the gas-solid reactions of the fuel, and impurities within the fuel, with oxygen carriers in order to determine reaction kinetics and chemical stability. To accomplish this it is important to know to what extent reactants, such as alkali, are in contact with the oxygen carrier particles, something which may be difficult if there is substantial effects of the reactor walls.

Here, we address the influence of reactor walls in CLC studies with a special focus on the behavior of alkali metal-containing compounds in laboratory-scale reactors. Small scale reactors and probe systems are often made of stainless steel and the reactor of interest in the present study is made of stainless-steel alloy 304. Regarding oxidation of this alloy, the literature suggests that both iron- and chromium oxide growth is present at high temperatures in alkali-containing environments [28–30]. Alkali losses in the oxidizing atmosphere can be explained by reactions between the potassium and chromium- and/or iron oxides to form K_2CrO_4 and $K_2Fe_2O_4$ [30–33]. In reducing atmosphere, the primary growth of the oxide layer is described as an outward growing iron rich layer and chromium rich inner layer at 600 °C [34]. At higher temperatures the oxide layer growth is expected to be dominated by Cr_2O_3 [28], while the oxygen activity is too low for iron oxides to be thermodynamically stable [35]. Numerous high temperature corrosion studies conclude that alkali can interact with the oxide layers on stainless-steel surfaces, and it has been observed that the presence of KCl can accelerate the reduction rate of iron oxides [36].

In the present study, we characterize alkali interaction with the inner wall of a laboratory-scale reactor for CLC studies. The aim is to evaluate the influence of wall processes on the reactor's performance, to improve current methodology for detailed studies of alkali-related processes in CLC and other applications. In the experiments, alkali in the form of KCl aerosol particles is continuously fed to the reactor and the concentrations of alkali, gases and aerosol particles are measured online during the experiments. The influence of alkali-wall interactions is investigated under recurring oxidizing, reducing and inert conditions at temperatures up to 900 °C, and the observations are related to the surface properties of stainless steel under oxidizing and reducing conditions. The observed wall effects are extensive and include major transient effects depending on gas composition, and the implications for laboratory studies and improved experimental methodology are discussed.

2. Experimental

2.1. Stainless-steel reactor

The laboratory-scale fluidized bed reactor used in the present study is depicted in Fig. 1. Similar types of reactors have been used in several earlier studies of CLC processes [37–41]. The reactor is made of stainless-steel (alloy 304). It has an inner diameter of 26 mm and a total length of 915 mm where the central part is heated to the desired operating temperature with an external electric heater. The reactor also contains a central particle filter and a thin plate gas distributor made of stainless steel (alloy 316) used to provide appropriate fluidization conditions. Note that no bed material was added in the present study that focuses on gas-wall effects.

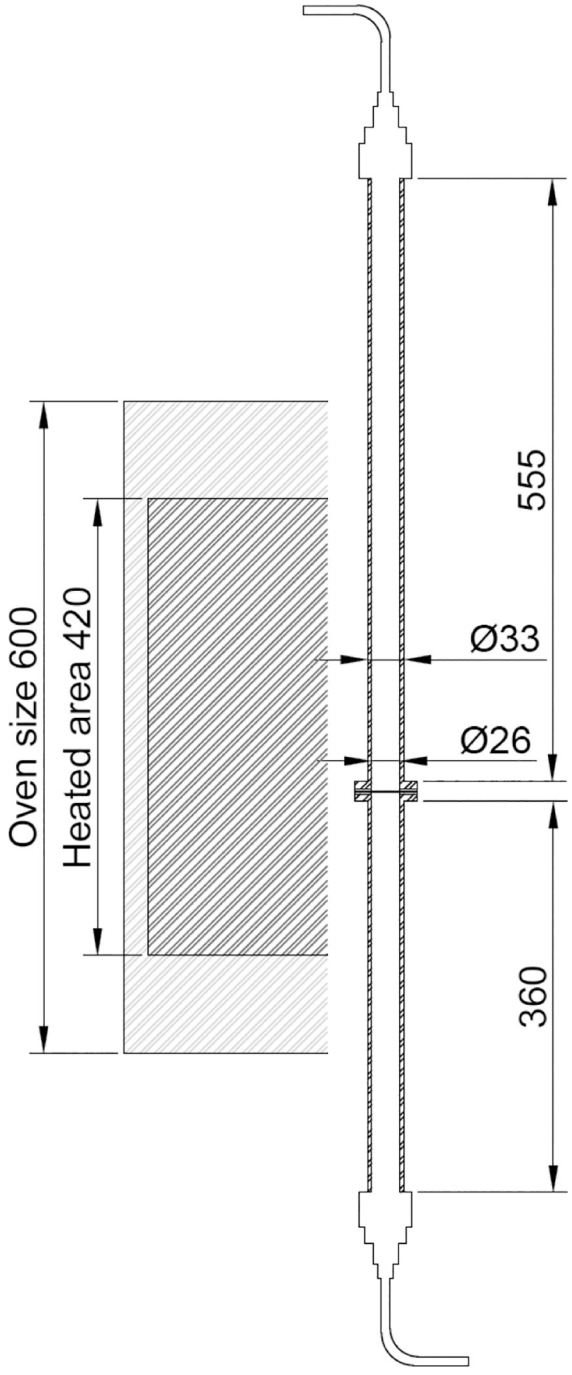

Fig. 1. Schematic overview of the stainless-steel reactor (dimensions in mm).

The wall material was analyzed with a scanning electron microscope (SEM; Phenom ProX Desktop SEM, Thermo Fisher Scientific Inc.), and the elemental composition (Table S1) was determined with energy-dispersive X-ray spectroscopy (EDS) by mapping (Fig. S1a) and line scan analysis (Fig. S1b). The material used for the SEM analysis was obtained by grinding from the top part of the reactor, which has not experienced high temperatures. The composition is in accordance with that of stainless-steel alloy 304, with the exception being a higher silica content (2.7 wt%) compared to what is generally seen in alloy 304 (1.0 wt%) [42]. No tendancy of element aggregation was seen in the analysis.

The reactor has been used for regular redox studies with oxygen carriers for approximately half a year before the present experiments, and earlier alkali loadings have been comparable to the ones used in the present study. The reactor has experienced experiments with durations of 3–4 h under oxidizing conditions (2.7 vol% O_2), which is expected to have formed a thin oxide scale on the reactor wall, while severe corrosion is neither expected nor observed. The reactor has also been opened and cleaned (water and soap) with no significant influence on the observations presented in this study.

2.2. Experimental setup

The experimental setup used for studies of alkali interactions with reactor walls under conditions that resemble those in a CLC system is shown in Fig. 2. The main components are an automated gas inlet system, a system for introduction of alkali to the reactor in the form of alkali salt aerosol particles, and instruments that characterize the gases and aerosol particles leaving the reactor.

A key to successful studies of alkali processes in biomass conversion systems is a stable and well-controlled alkali dosing system. We here introduce alkali to the reactor in the form of sub-micron alkali salt particles, a method that has previously proven successful in other studies [12,43]. The alkali salt particles were produced by the use of a commercial aerosol particle generator (Model 3076, TSI Inc.). In the particle generator a water solution containing the alkali salt of interest is atomized by expansion through an orifice using nitrogen as carrier gas, which results in an aerosol containing polydisperse droplets. The droplets then flow through an open path diffusion dryer (Model 3062, TSI Inc.) and exit as dry alkali salt particles at a relative humidity of approximately 20% [44]. The setup produces a stable and continuous aerosol output over several hours and the particle size is easily controlled by changing the concentration of the salt solution [43]. The present studies were carried out with KCl particles. The choice of KCl as alkali salt was based on the fact that biomass in general contains a relatively high concentration of potassium, which depending on the availability of chlorine normally forms highly volatile KCl under thermal conversion conditions [45]. The formed KCl particles had an average diameter of 45 nm in most of the present experiments, except the experiments where the effect of incident KCl concentration was investigated. The produced aerosol particles were transported through a conductive tube (inner diameter 8 mm, length 1.5 m), where losses to the walls can be ignored in the relevant size range [46], and the flow was mixed with the inlet gas flow before entering the reactor system.

The flow from the reactor is divided into three separate streams; one via a cooler and a particle filter to a gas analyzer, a second via a nitrogen diluter (dilution ratio of 10) to a surface ionization detector (SID) and scanning mobility particle sizer (SMPS), and a third to ventilation. The set-up makes it possible to carry out simulataneous online measurements of gas composition, particle and alkali concentrations.

A gas analyzer (Model NGA 2000, Emerson Electric Co.) was used to measure the concentrations of CO, CO_2, H_2, CH_4 and O_2. The SID used for online alkali measurements has been described in detail elsewhere [7,8,47,48]. The sample gas flows through the SID and a fraction of the alkali compounds in the flow dissociate and form alkali ions in contact with a hot platinum filament. The positively charged alkali ions leave the hot filament and diffuse to a nearby collector plate, where they

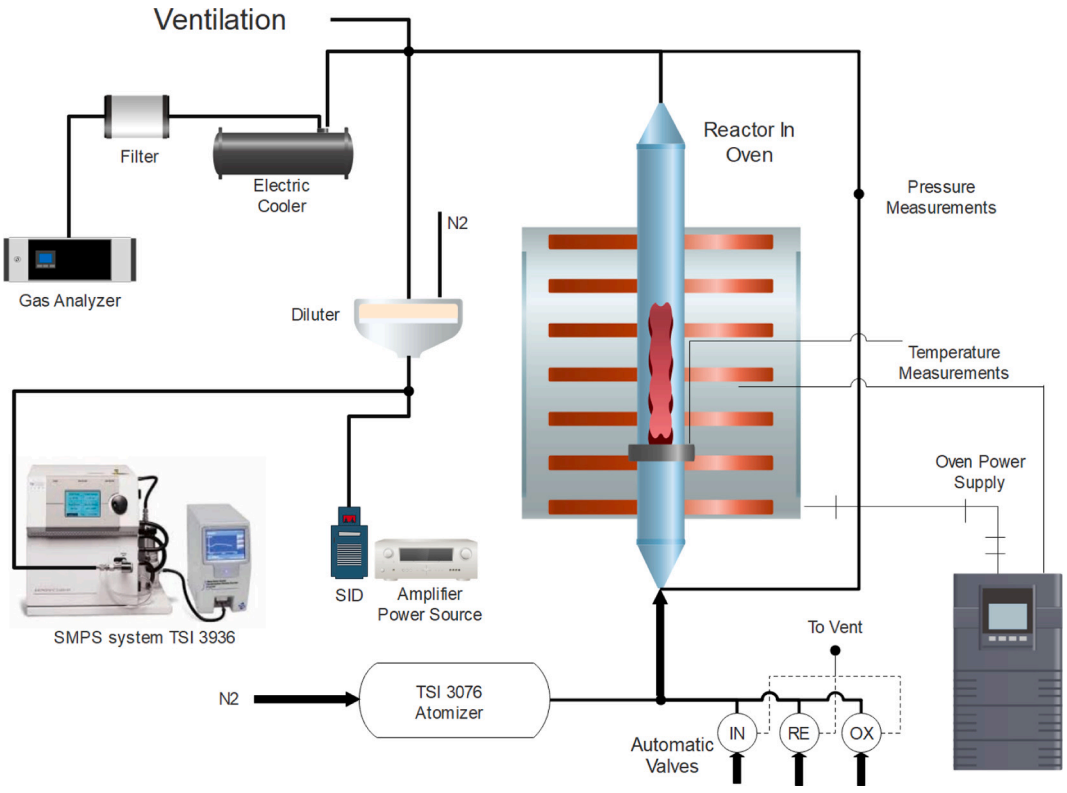

Fig. 2. Experimental set-up of the fluidized bed reactor placed in an oven and connected to an aerosol generator (Atomizer) and an automated gas-feeding system. Reactor exhaust gases flow via a diluter to an aerosol particle measurement system (SMPS) and a surface ionization detector (SID), and also through a cooler and filter to a gas analyzer.

produce a current proportional to the mass concentration of alkali in the gas flow. The instrument measures the total alkali concentration (K + Na) with a time resolution of typically 1 s. The technique has been applied in several earlier combustion and gasification studies [7,8,11,47,49]. The number concentration of aerosol particles was measured with a SMPS (Model 3936, TSI Inc.) that provided a complete scan of the 15–660 nm particle size range in 120 s.

2.3. Experimental procedure

The reactor was operated at a constant temperature of 800, 850 or 900 °C during the experiments, except for studies where a temperature ramp was applied. Three different gas atmospheres were used to mimic the conditions during biomass combustion in a CLC system. Inert conditions were provided using pure nitrogen as inlet gas. Oxidizing conditions were obtained using synthetic air (21% O_2 in N_2), and reducing conditions were simulated using synthetic fuel gas (50% H_2 and 50% CO). A gas flow of 0.3 L min^{-1} was mixed with an alkali-containing nitrogen flow of 2 L min^{-1} from the atomizer before entering the reactor, which resulted in gas concentrations during the experiments of either 2.7 vol% O_2 in N_2, or 6.5 vol% H_2 and 6.5 vol% CO in N_2. The use of 0, 5 or 10 mM KCl solutions in the atomizer resulted in KCl aerosol concentrations of 0, 6 and 12 mg m^{-3} after mixing with inlet gases, and the three cases are denoted “no alkali”, “medium loading” and “high loading”. Experiments were carried out with repeated redox cycles where each cycle consisted of the following subsequent stages: 180 s in an inert atmosphere, 1000 s in a reducing atmosphere, 500 s in an inert atmosphere, and 1450 s in an oxidizing atmosphere.

3. Results

3.1. Temperature dependence of alkali-reactor interactions

The influence of reactor temperature on gas, alkali and particle concentrations measured after the reactor are presented in Fig. 3. The experiments were carried out with a constant alkali flow into the reactor, and the gas composition was changed according to the repeated redox cycle described above to produce oxidizing, inert and reducing conditions. Reported values correspond to steady state values reached in each gas mixture.

Fig. 3a shows the observed alkali concentrations under oxidizing, inert and reducing conditions. Two cases are displayed for inert conditions depending on if they are preceded by an oxidizing or a reducing stage. The alkali concentration shows a similar dependence on gas composition at reactor temperature up to 600 °C, while a larger influence of the composition is observed at higher temperatures. Alkali losses are insignificant at room temperature, while some losses are observed as the temperature is increased to 400 °C. As further discussed below, KCl salt particles remain intact at these low temperatures and losses can be attributed to rapid particle diffusion in regions with steep temperature gradients. At 600 °C up to 92% of the alkali is lost in the reactor in all gas environments. At this temperature, KCl salt particles rapidly evaporate to form KCl(g). The diffusion rate of KCl in molecular form is several orders of magnitude higher than for the original aerosol particles. KCl molecules therefore rapidly reach the inner wall of the reactor where they adsorb and potassium remain for relatively long times compared to the time scale of the experiments. As the temperature increases further to 800 and 900 °C, alkali is increasingly released from the wall (41–74% of the alkali is lost at 900 °C) and a steady state alkali concentration is established in the reactor that depends on both temperature and gas composition. The gas composition changes the chemical composition of the surface layer of the wall. This affects the alkali desorption rate with the highest alkali release being observed under reducing conditions and in the inert stage that follows upon the reducing stage, while alkali release is substantially lower under oxidizing conditions.

The gas concentrations measured under the same conditions are presented in Fig. 3b. No gas conversion occurs at temperatures up to 400 °C. At 600 °C and above, CO is partially converted to CO_2 in the reducing environment. The observed fraction of $CO/CO_2 = 7$ and the additional oxygen likely originates from metal oxides in the surface layer of the stainless steel wall. A shift in H_2 concentration is also observed in the same temperature region. In the oxidizing and inert environments, no substantial changes in concentrations are observed in the investigated temperature range.

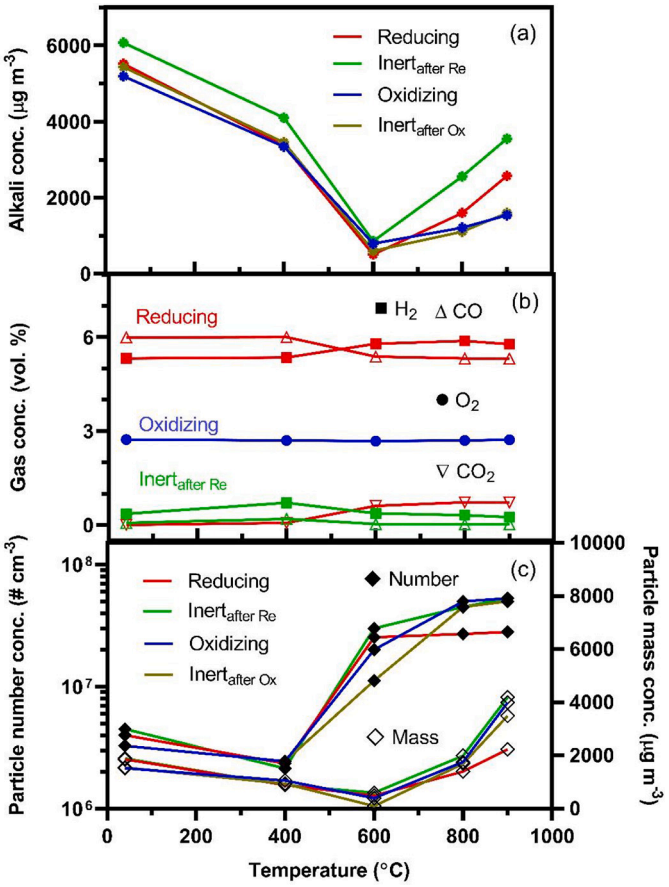

Fig. 3. (a) Alkali concentration, (b) gas concentrations and (c) particle number and mass concentrations as a function of reactor temperature. Measurements were conducted with medium alkali loading (6 mg m^{-3}), and with repeated redox cycles where the gas composition in each cycle is subsequently changed between oxidizing (blue lines and symbols), inert (bright green lines and symbols), reducing (red lines and symbols) and again inert (dark green lines and symbols) conditions. See text for further details.

Fig. 3c shows the total number concentration observed with a SMPS, together with particle mass concentrations. The mass concentrations have been calculated from the number concentrations assuming that all particles are spherical and have the bulk density of KCl (solid) (1.98 g cm^{-3}). The particle measurements at 25 °C and 400 °C show a relatively low number concentration that is consistent with the concentration produced by the particle generator, which indicates that the aerosol particles do not evaporate while passing through the system at these temperatures. The particle measurements at 600 °C show a rapid increase in number concentration and a large decrease in mass concentration. The changes in mass concentration are qualitatively comparable to the observations for alkali (Fig. 3a), although the influence of gas composition does not follow the same trend. The enhanced number concentration at high temperatures is an indication of newly nucleated particles. Compared to the particles leaving the aerosol generator, newly nucleated particles have a smaller diameter and are greater in number. Therefore, it is evident that the alkali particles evaporate at high

temperature and the alkali compounds nucleate to again form aerosol particles as the gas flow is cooled down on leaving the hot reactor. The total number concentrations may be affected by some particles being too small to be detected by the SMPS (lower limit approx. 15 nm).

A kinetic model has recently been shown to provide a semi-quantitative description of alkali salt particles undergoing evaporation under conditions resembling those in the present study [12]. The model describes the evaporation of an aerosol particle consisting of a single component, and takes into account the Kelvin effect that describes the increase in vapor pressure over a curved surface compared to a flat surface, while re-condensation of evaporated gas is ignored [12]. Fig. 4 shows the results when the model is applied to evaporation of 45 nm KCl particles in the present reactor system (reactor length of 420 mm, inner diameter of 26 mm, gas flow rate at room temperature of 2.3 L min^{-1}). The model considers changes in volumetric flow rate, and therefore changes in residence time in the reactor, as a function of temperature. The diameter of the transmitted KCl particles decreases rapidly with increasing temperature above 450 °C and particles evaporate completely before exiting the reactor at temperatures above 500 °C. The model results are consistent with the experimentally observed drop in alkali concentration when the temperature increases from 400 to 600 °C (Fig. 3a).

We next estimate the probability that KCl particles and molecules are able to penetrate the reactor without interacting with the reactor wall. As described above, 45 nm KCl particles are expected to rapidly evaporate in the 450–500 °C temperature range. The behavior of aerosol particles in the reactor is therefore considered at temperatures below 500 °C, while the behavior of KCl in molecular form is relevant above 500 °C.

The penetration, ***P,*** of aerosol particles through a reactor in a laminar flow can be calculated as a function of a dimensionless deposition parameter μ (with an accuracy of 1% for all values of μ) using the following empirical equations [46],

$$P = 1 - 5.50\mu^{2/3} + 3.77\mu \quad \text{for } \mu < 0.009$$
$$P = 0.819\,exp(-11.5\mu) + 0.0975\,exp(-70.1\mu) \quad \mu \geq 0.009 \tag{1}$$

$$\mu = DL/Q \tag{2}$$

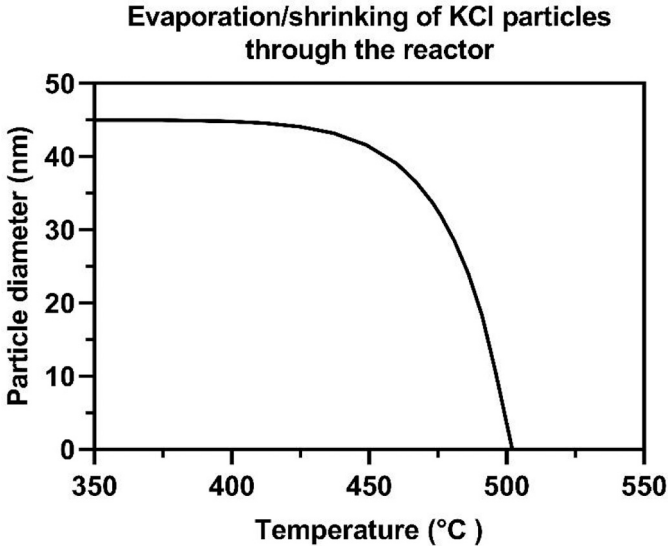

Fig. 4. Calculated shrinking of KCl particles, with an original diameter of 45 nm, as a function of reactor temperature. The calculations were carried out with the kinetic evaporation model and parameter values for KCl described in [12]. The length of the reactor was set to 0.42 m, which corresponds to the heated section of the reactor (see Fig. 1).

where D ($m^2 \cdot s^{-1}$) is the diffusion coefficient of KCl particles, L (m) is the reactor length and Q ($m^3 \cdot s^{-1}$) is the volumetric flow rate. Diffusion constants for 45 nm KCl particles are 4.2×10^{-5} $cm^2 \cdot s^{-1}$ at 25 °C and 1.3×10^{-4} $cm^2 \cdot s^{-1}$ at 500 °C. These were calculated with the Stokes-Einstein equation for diffusion coefficient of aerosol particles [46],

$$D = \frac{k_B T C_c}{3\pi\eta d_p} \tag{3}$$

where k_B ($m^2 \cdot kg \cdot s^{-2} \cdot K^{-1}$) is the Boltzmann constant, T (K) is the temperature, C_c is the dimensionless Cunningham correction factor, η (Pa • s) is the viscosity and d_p (m) is the particle diameter.

$$C_c = 1 + \frac{\lambda}{d_p}\left[2.34 + 1.05exp\left(-0.39\frac{\lambda}{d_p}\right)\right] \tag{4}$$

where λ (m) is the mean free path. KCl particles with a size of 45 nm will thus follow the laminar gas flow with minimal wall losses at both 25 and 500 °C. Compared to particles, the transmission of KCl molecules through the reactor quickly plummets [50]. This is expected since the diffusion coefficients for mulecules can be several orders of magnitude higher than those for particles. We conclude that the KCl molecules will rapidly reach the wall at temperatures above 500 °C [50].

Depending on the alkali desorption rate from the wall a steady state concentration of potassium builds up in the reactor at high temperatures. As the gas exits the externally heated section of the reactor, the temperature decreases. The drop in temperature results in nucleation of alkali aerosol particles that grow to a size that depends on the concentration of condensable material. The number concentration of newly formed particles is determined by the kinetics of the nucleation process and is typically in the order of 10^8 cm^{-3} [35], in agreement with the results displayed in Fig. 3c. Formation of new potassium-containing particles competes with condensation of on cold parts of the reactor wall, but in practice the total surface area of newly formed particles exceeds the wall surface area and condensation on cold walls play a minor role.

The newly formed particles are smaller than the original particles entering the reactor, due to the fact that the available condensable material is distributed over a larger total number of particles, and that some of the available potassium may have been lost to the inner reactor wall. The particle diffusion coefficient increases rapidly with decreasing particle size below 10 nm [35], and losses due to diffusion should be considered in a more detailed treatment. In addition, temperature gradients in the exiting flow tend to transport particles towards the cold walls [35], which may also result in losses.

3.2. *Influence of repeated redox cycles*

Each experiment consists of repeated redox cycles where the gas composition in subsequent steps changes between inert (180 s), reducing (800 s), inert (300 s) and oxidizing (800 s) conditions. Results from an experiment with five consecutive redox cycles at a reactor temperature of 900 °C are shown in Fig. 5. The observed changes in alkali and gas concentrations are highly reproducible between redox cycles. High reproducibility has also been observed between different experiments with the same operating parameters. Gas concentrations change according to expectations during the various stages, with some time required for a new steady state to be established after each change in gas composition. The alkali concentration is also highly reproducible between redox cycles, and intriguingly large transients are observed in connection with changes in gas composition.

One of the redox cycles in Fig. 5 is depicted in greater detail in Fig. 6. The figure contains colored areas that indicate reducing (orange), oxidizing (blue) and inert (white) conditions. Gas concentrations typically relax to new conditions in about 100 s or less. Minor transient changes in alkali concentration are observed in connection with changes from inert to oxidizing atmosphere, and again when switching back to

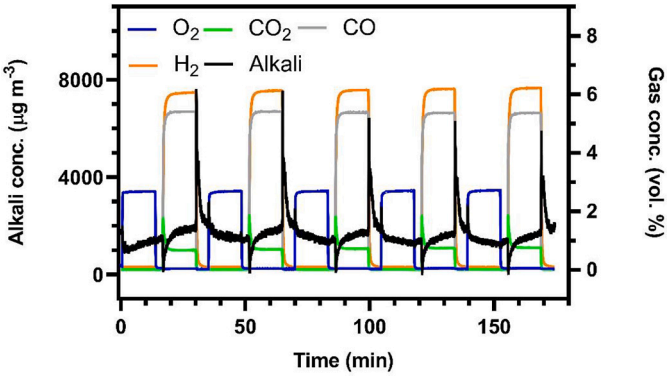

Fig. 5. Gas and alkali concentrations measured during five consecutive redox cycles at a reactor temperature of 900 °C and using medium alkali loading.

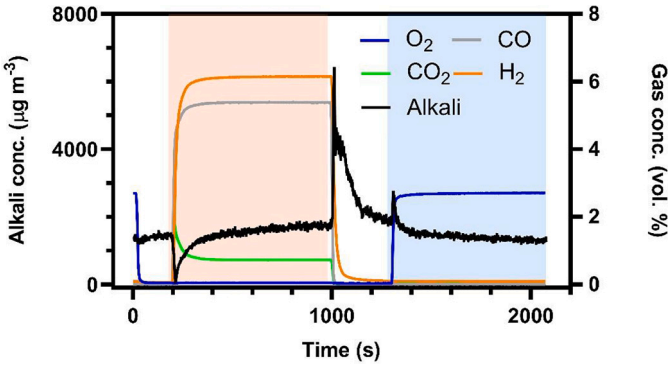

Fig. 6. Gas and alkali concentrations measured during one redox cycle at a reactor temperature of 900 °C and using medium alkali loading. Colored fields mark time periods with reducing (orange), oxidizing (blue) and and inert (white) conditions.

inert conditions. In contrast, pronounced transients are observed when reducing conditions are turned on and off. The alkali concentration decreases rapidly when reducing gases are being introduced, and the concentration recovers after about 200 s and thereafter slowly approaches a steady level around 2000 μg m^{-3}. When the gas composition is switched back to inert, the system responds with a major alkali release that over time decreases and approaches the preceding level.

3.3. Alkali loading effects at high reactor temperatures

Measurements were conducted with different alkali loadings by changing the KCl concentration in the solution reservoir in the aerosol generator, and concentrations of 0, 6 and 12 mg m^{-3} are denoted "no alkali", "medium loading" and "high loading". The used loadings are comparable to alkali concentrations of 1–35 mg m^{-3} measured during chemical-looping combustion of different types of biofuels in a 100 kW pilot [11]. In contrast, higher alkali concentrations have been reported during biomass gasification, including values of 20–60 mg m^{-3} during operation of a 32 MW_{th} dual fluidized bed (DFB) gasifier [7], and 30–250 mg m^{-3} in a pilot-scale 2–4 MWth DFB gasifier [8].

Experiments were carried out using the three different alkali loadings at constant reactor temperatures of 800, 850 and 900 °C, and the resulting alkali concentrations are presented in Fig. 7 where colored areas indicate reducing (orange), oxidizing (blue) and inert (white) conditions. Results for the case with no alkali injection as expected show low concentrations of alkali (Fig. 7a). The alkali levels are overall low at 800 and 850 °C and slightly higher at 900 °C, and the likely origin is a minor release of alkali from the wall material. Small increases in intensity are observed when switching between gas compositions, with the highest peaks being observed when switching from reducing to inert conditions.

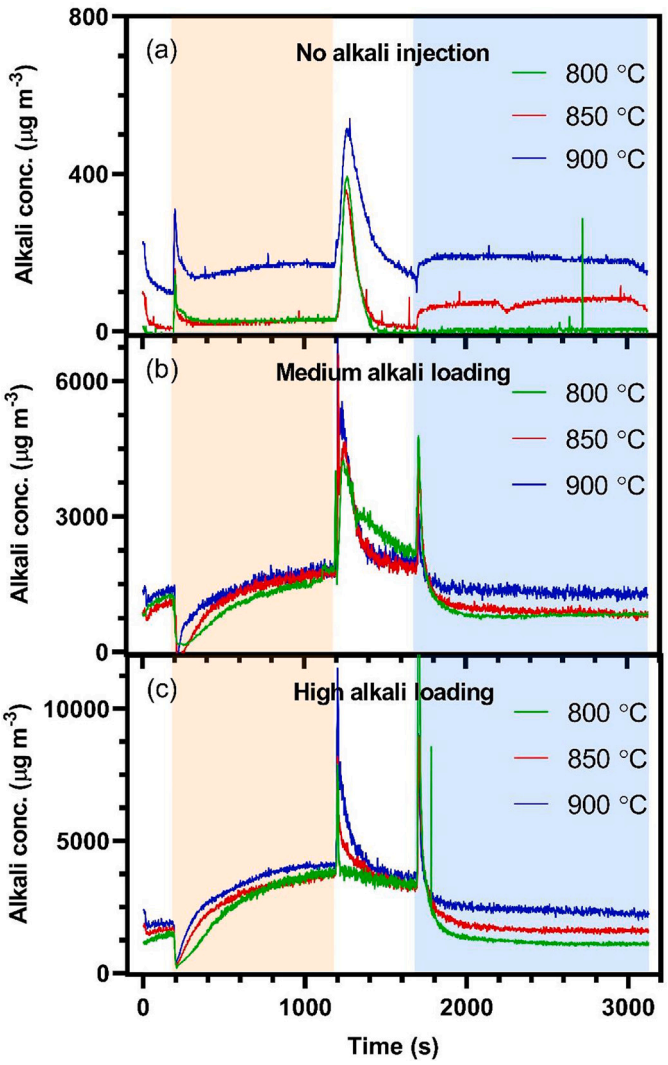

Fig. 7. Alkali concentrations measured in experiments with different inlet KCl concentrations: (a) no alkali injection, (b) medium alkali loading and (c) high alkali loading. Results are displayed for reactor temperatures of 800, 850 and 900 °C. Colored fields mark time periods with reducing (orange), oxidizing (blue) and and inert (white) conditions.

The medium alkali loading case corresponds to the standard case used in Figs. 3,5 and 6, and results obtained at three different temperatures are compared in Fig. 7b. A similar pattern is observed during the redox cycle at all three temperatures, with only minor differences depending on temperature. A rapid drop in alkali concentration is observed when reducing gases enter the reactor, and the subsequent signal recovery appears to occur faster with increasing temperature. The highest alkali peak during the following inert stage also appears to change with temperature, while the final oxidizing stage displays an increased alkali level at 900 °C compared to the lower temperatures.

The corresponding results using a high loading are shown in Fig. 7c. The results in general confirm the trends observed with medium loading, but also display some unique features and the increased loading does not simply change the absolute alkali level. This is, in particular, true for the alkali peak during the inert stage that displays a pronounced change in intensity as well as kinetics with increasing temperature.

4. Discussion

4.1. High temperature behavior of alkali-containing molecules and aerosol particles

The present study highlights the need to carefully consider the behavior of alkali-containing compounds in thermal conversion processes. Before focusing on alkali-wall interactions in the next section, we first address the importance of aerosol processes and thermal stability of alkali compounds.

The fact that alkali salts are in the condensed state up to several hundred degrees makes it possible to dose alkali compounds in the form of aerosol particles into a reactor system. The low diffusion coefficient of aerosol particles with sizes of tens of nanometers and larger make them follow the gas streams with no or very limited losses [35]. This is in general true for particles with a diameter up to a few micrometers, where losses by impaction become increasingly important with increasing particle size [35]. The use of aerosol particles is thus a convenient method to dose alkali into a reactor over a wide concentration range, and the present study is an illustrative example of this method.

The advantages of handling alkali compounds in the form of aerosol particles are again apparent when gaseous alkali compounds leave a reactor and form particles by nucleation or condensation on existing particles. These particles are then transported and detected with existing aerosol science methods.

The conditions change dramatically when aerosol particles experience high enough temperatures to evaporate. The behavior of alkali compounds in molecular form is very different from the behavior of aerosol particles, and one important aspect is the diffusion coefficient that is several orders of magnitude higher for molecules. As shown in the present study, this effect increases their interaction with any available surfaces including fluidized bed particles, oxygen carriers in CLC processes, reactor walls and gas extraction probes used in pilot- and industrial-scale studies, which leads us to a discussion of alkali-surface interactions in the following.

4.2. Chemistry of alkali-wall interactions

To further interpret the experimental results, the conditions at the surface of the stainless steel wall need to be considered. It is well known that chromium and iron in stainless steel alloys form a thin oxide scale under dry and oxidizing conditions [28–31]. The scale forms at 600–700 °C and consists of a $(Cr_xFe_{x-1})_2O_3$ inner layer with about 70% chromium and an iron-rich outer part. Huntz et al. showed that for temperatures between 850 and 950 °C, the formed oxide scale mainly consists of chromium oxide (Cr_2O_3), and at 950 °C, iron oxide is particularly important [28]. Chromium in solution also exhibits a higher tendency to become internally oxidized in the presence of water vapor because of hydrogen dissolution in the alloy [51]. This mechanism explains why Fe—Cr alloys with 10–20 wt% Cr exhibit protective chromium-rich scale in dry gases, but tend to form breakaway-type Fe-rich oxides in wet gases [51].

The number of studies performed in environments with a low oxygen activity is significantly smaller [34,52–55]. In a reducing atmosphere at 600 °C, the primary growth of the oxide layer on stainless-steel 304 L has been described as an outward growing iron rich layer and chromium rich inner layer [34]. The initial (up to 1 h) oxide is, however, rich in chromium and continued growth is due to an outward growing iron rich oxide layer [34]. At higher temperatures (850–900 °C) and low oxygen activity, the oxide layer in reducing atmosphere is expected to be dominated by Cr_2O_3 [28]. This conclusion is based on Ellingham theory which relates the oxygen activity in the reactor to the stable oxide. In the present study, the CO/CO_2 ratio is around 6.8 in reducing atmosphere at 800–900 °C. This corresponds to approximate oxygen activities $pO_2 = 10^{-20}$, 10^{-19} and 10^{-18} atm at 800, 850 and 900 °C, respectively [35], and the metal oxides predicted to form are listed in Table 1. According to Ellingham theory Cr_2O_3 is formed under the present reducing conditions, while nickel- or iron oxide is not. It should be noted that Ellingham theory is based on the thermodynamics of pure substances and does not consider kinetics or addition of corrosive agents like alkali chlorides.

To support the description of the stainless steel a phase diagram for a simplified version of Alloy 304 was simulated using FactSage 7.2®, FactSage is an integrated database computing system which uses calculation modules with access to different solution databases and substances. The Equilib module used here is based on a Gibbs energy minimization and the assumption of chemical equilibrium for each thermodynamic state. The Equilib input data was 70 wt% Fe, 20 wt% Cr and 10 wt% Ni, and the temperature was varied between 300 and 1000 °C and the O_2 partial pressure between 10^{-21} and 10^{-1} atm. The databases included in the calculation were FactPS, FToxid and FTmisc.

The calculated phase diagram is shown in Fig. 8 and the chemical composition of the individual phases is listed in Table 2. The thermodynamic calculations predict similar oxidation products as discussed above. Corundum $((Fe,Cr)_2O_3)$ and spinel $(Fe,Cr,Ni)_3O_4$ are predicted to be stable in oxidizing conditions. The iron oxides are gradually reduced when the oxygen activity is lowered and the main products are Cr_2O_3 and fcc (Ni and Fe in their metallic crystalline structure) at the lowest O_2 partial pressure. However, in contrast to the results using Ellingham theory [35], the phase diagram suggests that iron oxides are still present under the reducing conditions used in this study (red marks in Fig. 8). Important to note is that neither FactSage nor Ellingham calculations have taken the presence of alkali into account, which has been shown to affect the reduction of iron oxides [36].

It is less clear how KCl interacts with and influences the surface structures formed under oxidizing and reducing conditions. Corrosion in oxidizing conditions may be initiated by the reaction of KCl with the chromium-containing oxide to produce potassium chromate particles, leaving a chromium-depleted oxide on the alloy surface [30]. The rapid oxidation results in a thick scale of a mixture of hematite ($(Fe,Cr,Ni)_2O_3$), spinel oxide ($(Fe,Cr,Ni)_3O_4$) and K_2CrO_4 [30,32]. When iron oxide is present on the surface $K_2Fe_2O_4$ may also form [31], and the potassium reactions with chromium- and/or iron oxides may be summarized by the following reactions [30–32],

$$4KCl + Cr_2O_3(s) + 5/2O_2(g) + 4e^- \rightarrow 2K_2CrO_4(s) + 4Cl^- \quad (5)$$

$$4KCl(s) + Cr_2O_3(s) + 5/2O_2(g) \rightarrow 2K_2CrO_4(s) + 2Cl_2(g) \quad (6)$$

$$2KCl(g) + Fe_2O_3(s) + 1/2O_2(g) \rightarrow K_2Fe_2O_4(s) + Cl_2(g) \quad (7)$$

The formed chloride ions and molecular chlorine may continue to form volatile metal chlorides by the following processes (M = Fe, Cr, Ni) [56]:

$$M^{2+} + 2Cl^- \rightarrow MCl_2(s) \quad (8)$$

$$M(s) + Cl_2(g) \rightarrow MCl_2(s) \quad (9)$$

$$MCl_2(s) \rightarrow MCl_2(g) \quad (10)$$

Table 1
Partial pressure of oxygen needed to form specific oxides in stainless steel at different temperatures according to Ellingham data [35].

Oxide formation	pO_2 at 800 °C (atm)	pO_2 at 850 °C (atm)	pO_2 at 900 °C (atm)
$4Fe_3O_4 + O_2 = 6Fe_2O_3$	10^{-9}	10^{-8}	10^{-7}
$2Ni + O_2 = 2NiO$	5×10^{-15}	5×10^{-14}	5×10^{-13}
$6FeO + O_2 = 2Fe_3O_4$	10^{-17}	10^{-16}	5×10^{-15}
$2Fe + O_2 = 2FeO$	10^{-19}	10^{-18}	10^{-17}
$4Cr + 3O_2 = 2Cr_2O_3$	10^{-27}	10^{-25}	10^{-24}

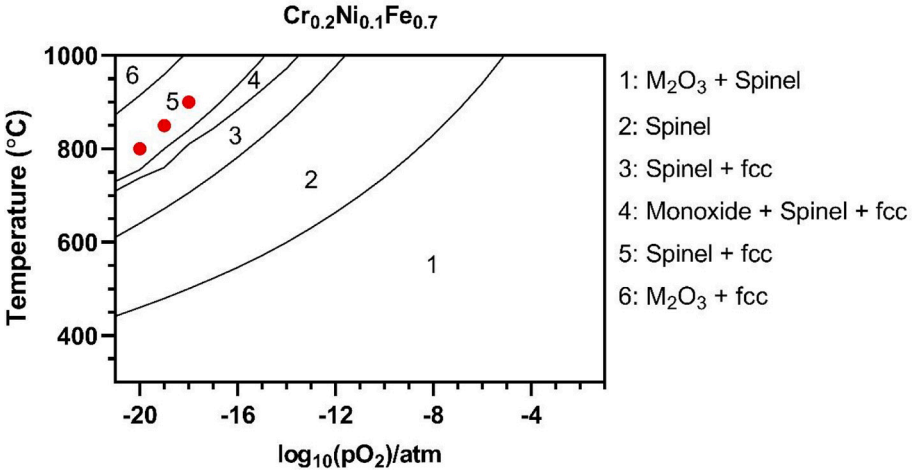

Fig. 8. Phase diagram of a simplified composition of stainless-steel 304 calculated with FactSage 7.2. Red symbols mark the reducing conditions at 800, 850 and 900 °C used in this study. Where fcc means face centered cubic and describes the crystalline structure of the material.

Table 2
Chemical components in the different areas of the phase diagram in Fig. 8 based on calculations using FactSage 7.2. All phases and chemical compositions are reported in wt%.

Area	Wt %	Compound	Wt %	Compound	Wt %	Compound
1	**70**	**M_2O_3**	**30**	**Spinel**		
	76	Fe_2O_3	51	$FeNi_2O_4$		
	24	Cr_2O_3	30	Fe_3O_4		
			19	$FeCr_2O_4$		
2		**Spinel**				
	54	Fe_3O_4				
	31	$FeCr_2O_4$				
	15	$FeNi_2O_4$				
3 = 5	**38**	**Spinel**	**62**	**fcc**		
	99	$FeCr_2O_4$	86	Fe		
	1	Fe_3O_4	14	Ni		
4	**31**	**Monoxide**	**56**	**Spinel**	**13**	**fcc**
	83	FeO	58	$FeCr_2O_4$	57	Ni
	15	Fe_2O_3	42	Fe_3O_4	43	Fe
	2	Cr_2O_3				
6	**26**	**M_2O_3**	**74**	**fcc**		
		Cr_2O_3	87	Fe		
			13	Ni		
Higher T, Lower p (O_2)		**fcc**				
	70	Fe				
	20	Cr				
	10	Ni				

$$4MCl_2(g) + 3O_2(g) \rightarrow 2M_2O_3(s) + 4Cl_2(g) \quad (11)$$

where the subsequent formation of metal oxides by Reaction (11) again releases chlorine that may continue to react.

Studies reporting high temperature corrosion of stainless steels in low oxygen environments containing alkali are scarce. Nakagawa et al. reported that addition of KCl(g) increases the reduction rate of iron oxide due to the formation of porous products that promotes further reaction [36]. In addition, Lehmusto et al. [32] have suggested that potassium chloride and chromium oxide undergo the following reaction in an environment with low oxygen activity environment and available water vapor:

$$2KCl(s) + Cr_2O_3(s) + H_2O(g) \rightarrow K_2CrO_4(s) + 2HCl(g) \quad (12)$$

We next relate the expected surface properties of the steel to the experimental results from the present study. Starting with oxidizing conditions, the gas phase alkali concentration is observed to reach a steady state in approximately 100 s in the beginning of the oxidizing stage of the redox cycle. The short time scale indicates that any changes are dominated by processes in the uppermost surface layer. The changes also appear to be reversible on the time scale of the experiments and including repeated redox cycles. In steady state, the flow of alkali from the gas phase is balanced by alkali evaporation from the steel surface, which is expected to consist of iron and chromium oxides [28–31]. The gas phase alkali concentration is seen to increase with increasing temperature (see Fig. 7b and c), and using the observed alkali levels for the high alkali loading case (Fig. 7c) an apparent heat of sublimation of 80 ± 15 kJ mol^{-1} may be calculated. Further studies with alternative methods are needed to reveal additional details about the surface state of potassium on the oxidized surface, including the potential role of $K_2Fe_2O_4$ and/or $K_2Cr_2O_4$ [30–32].

The surface conditions appear to be relatively stable also during the inert phase that follows on the oxidizing stage, but changes drastically when reducing conditions are applied. The alkali concentration drops sharply in the beginning of the reducing stage, and then slowly recovers to a higher level during a few hundred seconds. At the same time CO_2 production peaks (Fig. 6), and decreases to a lower level on a similar time scale as the changes observed for alkali. This is consistent with a reduction of the surface oxide layer, and thus agrees with the expected structural changes under reducing conditions discussed above [34,52–55]. The reduction of the surface layer obviously provides binding sites for potassium that is transiently lost to the newly formed surface. However, the kinetics are slowed down after the initial changes and growth of a potassium-rich phase is limited on longer time scales. The existing literature would suggest the formation of $K_2Cr_2O_4$ [32], but further studies are needed to identify the responsible surface state. Interestingly, the newly formed alkali-containing phase appears only to be stable under reducing conditions, since a sharp rise in alkali concentration is observed when switching back to inert conditions.

The transient loss of KCl when changing from inert to reducing conditions can be estimated to approximately 8.4 μg (medium alkali loading; 850 °C) based on the reactor flow and the alkali levels before and after the transient change. The total geometric surface area in the actively heated part of the reactor is 343 cm^2 (reactor length of 420 mm; inner diameter of 26 mm). Using these values the average loss to the hot inner surface corresponds to $2 \cdot 10^{14}$ KCl molecules cm^{-2}, or 0.2 monolayers (ML) assuming a typical value of $\sim 1 \cdot 10^{15}$ cm^{-2} for a complete ML. Note that this is an upper estimate since the actual surface area is larger than the geometric area, and KCl losses to other parts of the reactor have been ignored. The transient alkali release when changing from reducing to inert conditions is in a similar way estimated to 12.2 μg (medium alkali loading; 850 °C), and is thus similar to the alkali loss during the preceding stage.

4.3. Implications for laboratory-scale thermal conversion studies

The obvious outcome of this investigation is the understanding that wall interactions need to be taken into account when studying the behavior of alkali compounds in CLC processes. The employed reactor may be considered a standard setup for laboratory-scale fluidized bed studies. In the present case, the alkali concentration is observed to vary between 0 and 12 mg m^{-3} (high alkali loading) depending on the surface properties of the wall. Although alkali is introduced in a controlled way, the actual alkali concentration interacting with a bed of oxygen carrier particles is largely set by the surface properties of the reactor wall. The effects are large and can easily obscure any signature of alkali interactions with the oxygen carriers themselves.

On a positive note, the present study shows that experimental conditions with high reproducibility can be maintained which helps separate the effects of oxygen carriers and walls, and highly valuable information may be obtained even though the influence of different factors cannot be separated under all circumstances. Other options are related to changes in material and geometry of the reactor. Another reactor material may perform better than stainless steel depending on the reactivity in oxidizing and reducing conditions. Although the high temperature properties under oxidizing conditions may be well known reducing conditions may be incompletely studied, and in practice separate studies of alkali-material interactions may be required to find a superior material.

Another option is to reduce the hot wall area that directly interacts with the system of interest. It may be difficult to completely avoid alkali-wall interactions, but they may be considerably limited compared to the present setup. Of particular relevance is the use of steep temperature gradients that promote the formation of aerosol particles before gaseous alkali compounds reach the wall. A second favorable factor is that the large total surface area within a fluidized bed may be orders of magnitude larger than the area of an adjacent reactor wall.

In general, we argue that alkali-wall interactions need to be carefully considered in any experiment aiming at a deeper understanding of alkali processes in thermal conversion. We also note that the present methodology may shed new light on alkali corrosion and catalytic effects under high temperature conditions. There are also several possibilities for additional experiments that may help understand the specific surface processes on the steel surfaces investigated here, including systematic changes in CO, H_2, H_2O, and experiments with other alkali compounds including KOH that can be expected to be common in thermal conversion processes.

5. Conclusions

Experiments have been performed to evaluate the influence of alkali interactions with the inner wall of a laboratory-scale reactor for CLC studies. Alkali in the form of KCl aerosol particles was continuously introduced to the reactor and the influence of alkali-wall interactions was investigated at temperatures up to 900 °C under oxidizing, reducing and inert conditions. The main conclusions can be summarized as follows:

- The introduced aerosol particles evaporate at temperatures above 500 °C and rapidly diffuse to the inner wall of the reactor in molecular form. Alkali reaching the wall largely remains adsorbed at temperatures below 700 °C, while re-evaporation is important at higher temperatures.
- The gas composition affects the observed alkali concentrations and large transient effects are observed when changing gas composition during repeated redox cycles.
- The observed effects are linked to chemical transformations in the surface layer of the stainless steel wall material, which take place on a time scale of a few hundred seconds.
- The reduction of metal oxides in the surface layer allows for the formation of a new potassium-rich phase, which appears to be stable in a reducing atmosphere but not under inert conditions.
- It is concluded that alkali-wall interactions need to be carefully taken into account when studying the behavior of alkali compounds in CLC processes, and in other experiments aiming at a detailed understanding of alkali processes in thermal conversion.

Based on the present findings, work is currently underway to develop new types of reactors for the investigation of alkali interactions with oxygen carriers used in CLC.

Declaration of Competing Interest

The authors declare no conflict of interest.

Acknowledgments

This work is supported by the Swedish Research Council, project “Biomass combustion chemistry with oxygen carriers” 2016-06023. We gratefully acknowledge the assistance from Ivana Staničić in carrying out FactSage calculations, and from Biniam Kifleyesus during SEM studies.

Appendix A. Supplementary data

Supplementary data to this article can be found online at https://doi.org/10.1016/j.fuproc.2021.106828.

References

[1] G. Myhre, D. Shindell, F.-M. Bréon, W. Collins, J. Fuglestvedt, J. Huang, D. Koch, J.-F. Lamarque, D. Lee, B. Mendoza, T. Nakajima, A. Robock, G. Stephens, T. Takemura, H. Zhang, Anthropogenic and natural radiative forcing, in: T. F. Stocker, D. Qin, G.-K. Plattner, M. Tignor, S.K. Allen, J. Boschung, P.M. Midgley (Eds.), Climate change 2013: the physical science basis. Contribution of Working Group I to the Fifth Assessment Report of the Intergovernmental Panel on Climate Change, Cambridge University Press, Cambridge, United Kingdom and New York, NY, USA, 2013.
[2] J.K. Filip Johansson, Mikael Odenberger, the importance of CO2 capture and storage: a geopolitical discussion, Therm. Sci. 16 (2012) 655–668.
[3] C. Azar, D.J.A. Johansson, N. Mattsson, Meeting global temperature targets—the role of bioenergy with carbon capture and storage, Environ. Res. Lett. 8 (2013), 034004.
[4] R.S. Haszeldine, Carbon Capture and Storage: how Green can Black be? Science 325 (2009) 1647.
[5] P. Hallberg, M. Hanning, M. Rydén, T. Mattisson, A. Lyngfelt, Investigation of a calcium manganite as oxygen carrier during 99 h of operation of chemical-looping combustion in a 10 kWth reactor unit, Int. J. Greenhouse Gas Control 53 (2016) 222–229.
[6] S. Heidenreich, P.U. Foscolo, New concepts in biomass gasification, Prog. Energy Combust. Sci. 46 (2015) 72–95.
[7] D. Gall, M. Pushp, A. Larsson, K. Davidsson, J.B.C. Pettersson, Online measurements of alkali metals during start-up and operation of an industrial-scale biomass gasification plant, Energy Fuel 32 (2018) 532–541.
[8] M. Pushp, D. Gall, K. Davidsson, M. Seemann, J.B.C. Pettersson, Influence of bed material, additives, and operational conditions on alkali metal and tar concentrations in fluidized bed gasification of biomass, Energy Fuel 32 (2018) 6797–6806.
[9] H. Thunman, F. Lind, C. Breitholtz, N. Berguerand, M. Seemann, Using an oxygen-carrier as bed material for combustion of biomass in a 12-MWth circulating fluidized-bed boiler, Fuel 113 (2013) 300–309.
[10] M. Zevenhoven, P. Yrjas, M. Hupa, Ash-Forming Matter and Ash-Related Problems, in, 2010.
[11] I. Gogolev, C. Linderholm, D. Gall, M. Schmitz, T. Mattisson, J.B.C. Pettersson, A. Lyngfelt, Chemical-looping combustion in a 100 kW unit using a mixture of synthetic and natural oxygen carriers – Operational results and fate of biomass fuel alkali, Int. J. Greenhouse Gas Control 88 (2019) 371–382.
[12] D. Gall, M. Pushp, K.O. Davidsson, J.B.C. Pettersson, Online measurements of alkali and heavy tar components in biomass gasification, Energy Fuel 31 (2017) 8152–8161.
[13] A.A. Khan, W. de Jong, P.J. Jansens, H. Spliethoff, Biomass combustion in fluidized bed boilers: potential problems and remedies, Fuel Process. Technol. 90 (2009) 21–50.
[14] M. Öhman, A. Nordin, B.-J. Skrifvars, R. Backman, M. Hupa, Bed agglomeration characteristics during fluidized bed combustion of biomass fuels, Energy Fuel 14 (2000) 169–178.

[15] A. Corcoran, J. Marinkovic, F. Lind, H. Thunman, P. Knutsson, M. Seemann, Ash properties of ilmenite used as bed material for combustion of biomass in a circulating fluidized bed boiler, Energy Fuel 28 (2014) 7672–7679.
[16] I. Staničić, V. Andersson, M. Hanning, T. Mattisson, R. Backman, H. Leion, Combined manganese oxides as oxygen carriers for biomass combustion — Ash interactions, Chem. Eng. Res. Des. 149 (2019) 104–120.
[17] E. Björkman, B. Strömberg, Release of chlorine from biomass at pyrolysis and gasification conditions 1, Energy Fuel 11 (1997) 1026–1032.
[18] T. Mendiara, A. Abad, L.F. de Diego, F. García-Labiano, P. Gayán, J. Adánez, Biomass combustion in a CLC system using an iron ore as an oxygen carrier, Int. J. Greenhouse Gas Control 19 (2013) 322–330.
[19] E. Darwish, D. Yılmaz, H. Leion, Experimental and thermodynamic study on the interaction of copper oxygen carriers and oxide compounds commonly present in ashes, Energy Fuel 33 (2019) 2502–2515.
[20] F. Hildor, M. Zevenhoven, A. Brink, L. Hupa, H. Leion, understanding the interaction of potassium salts with an ilmenite oxygen carrier under dry and wet conditions, ACS Omega 5 (2020) 22966–22977.
[21] F. Störner, F. Hildor, H. Leion, M. Zevenhoven, L. Hupa, M. Rydén, Potassium ash interactions with oxygen carriers steel converter slag and iron mill scale in chemical-looping combustion of biomass—experimental evaluation using model compounds, Energy Fuel 34 (2020) 2304–2314.
[22] I. Gogolev, A.H. Soleimanisalim, C. Linderholm, A. Lyngfelt, Commissioning, performance benchmarking, and investigation of alkali emissions in a 10 kWth solid fuel chemical looping combustion pilot, Fuel 287 (2021) 119530.
[23] L. Shen, J. Wu, J. Xiao, Q. Song, R. Xiao, Chemical-looping combustion of biomass in a 10 kWth reactor with iron oxide as an oxygen carrier, Energy Fuel 23 (2009) 2498–2505.
[24] S.C. Bayham, H.R. Kim, D. Wang, A. Tong, L. Zeng, O. McGiveron, M.V. Kathe, E. Chung, W. Wang, A. Wang, A. Majumder, L.-S. Fan, Iron-based coal direct chemical looping combustion process: 200-h continuous operation of a 25-kWth subpilot unit, Energy Fuel 27 (2013) 1347–1356.
[25] J. Adánez, A. Abad, R. Perez-Vega, L.F. de Diego, F. García-Labiano, P. Gayán, Design and operation of a coal-fired 50 kWth chemical looping combustor, Energy Procedia 63 (2014) 63–72.
[26] C. Linderholm, M. Schmitz, M. Biermann, M. Hanning, A. Lyngfelt, Chemical-looping combustion of solid fuel in a 100kW unit using sintered manganese ore as oxygen carrier, Int. J. Greenhouse Gas Control 65 (2017) 170–181.
[27] J. Ströhle, M. Orth, B. Epple, Design and operation of a 1MWth chemical looping plant, Appl. Energy 113 (2014) 1490–1495.
[28] A.M. Huntz, A. Reckmann, C. Haut, C. Sévérac, M. Herbst, F.C.T. Resende, A.C. S. Sabioni, Oxidation of AISI 304 and AISI 439 stainless steels, Mater. Sci. Eng. A 447 (2007) 266–276.
[29] T. Jonsson, H. Larsson, S. Karlsson, H. Hooshyar, M. Sattari, J. Liske, J.E. Svensson, L.G. Johansson, High-temperature oxidation of FeCr(Ni) Alloys: the behaviour after breakaway, Oxid. Met. 87 (2017) 333–341.
[30] J. Pettersson, J.E. Svensson, L.G. Johansson, KCl-induced corrosion of a 304-type austenitic stainless steel in O2 and in O2 + H2O environment: the influence of temperature, Oxid. Met. 72 (2009) 159–177.
[31] S.C. Cha, M. Spiegel, Local reactions of KCl particles with iron, nickel and chromium surfaces, Mater. Corros. 57 (2006) 159–164.
[32] J. Lehmusto, P. And, Reactions of potassium chloride with chromium as a first step towards high temperature corrosion in biomass combustion, 2019.
[33] J. Lehmusto, M. Olin, J. Viljanen, J. Kalliokoski, F. Mylläri, J. Toivonen, M. Dal Maso, L. Hupa, Detection of gaseous species during KCl-induced high-temperature corrosion by the means of CPFAAS and CI-APi-TOF, Mater. Corros. 71 (2020) 222–231.
[34] H. Hooshyar, T. Jonsson, J. Hall, J.E. Svensson, L.G. Johansson, J. Liske, The effect of H2 and H2O on the oxidation of 304L-stainless steel at 600 °C: general behaviour (part I), Oxid. Met. 85 (2016) 321–342.
[35] A. Khanna, High Temperature Oxidation and Corrosion, 2002.
[36] H. Nakagawa, Y. Ono, Effects of potassium chloride on the reduction of iron oxides, Trans. Iron Steel Institute Japan 25 (1985) 1021–1024.
[37] F. Shen, J. Liu, Z. Zhang, Y. Yang, Temporal measurements and kinetics of selenium release during coal combustion and gasification in a fluidized bed, J. Hazard. Mater. 310 (2016) 40–47.
[38] M. Zevenhoven, C. Sevonius, P. Salminen, D. Lindberg, A. Brink, P. Yrjas, L. Hupa, Defluidization of the oxygen carrier ilmenite – Laboratory experiments with potassium salts, Energy 148 (2018) 930–940.
[39] C. Sevonius, P. Yrjas, D. Lindberg, L. Hupa, Impact of sodium salts on agglomeration in a laboratory fluidized bed, Fuel 245 (2019) 305–315.
[40] C. Sevonius, P. Yrjas, D. Lindberg, L. Hupa, Agglomeration tendency of a fluidized bed during addition of different phosphate compounds, Fuel 268 (2020) 117300.
[41] Z. Zhang, J. Liu, F. Shen, Z. Wang, Temporal release behavior of potassium during pyrolysis and gasification of sawdust particles, Renew. Energy 156 (2020) 98–106.
[42] T.W. Material, Grade 304 stainless steel properties, tensile yield strength, thermal conductivity, in, The World Material, https://www.theworldmaterial.com/type-304-grade-stainless-steel/.
[43] P.H. Moud, K.J. Andersson, R. Lanza, J.B.C. Pettersson, K. Engvall, Effect of gas phase alkali species on tar reforming catalyst performance: initial characterization and method development, Fuel 154 (2015) 95–106.
[44] P. Instruments, Model 3062 Diffusion Dryer - Instruction Manual, in, TSI, 2003.
[45] X. Li, F. He, X. Su, F. Behrendt, Z. Gao, H. Wang, Evaporation rate of potassium chloride in combustion of herbaceous biomass and its calculation, Fuel 257 (2019) 116021.
[46] H. WC, Aerosol Technology - Properties, Behavior and Measurement of Airborne Particles, Wiley, New York, 1999.
[47] K. Davidsson, K. Engvall, M. Hagström, J. Korsgren, B. Lönn, J. Pettersson, A surface ionization instrument for on-line measurements of alkali metal components in combustion: instrument description and applications, Energy Fuel 16 (2002).
[48] M. Hagström, K. Engvall, J.B.C. Pettersson, Desorption kinetics at atmospheric pressure: alkali metal ion emission from hot platinum surfaces, J. Phys. Chem. B 104 (2000) 4457–4462.
[49] J. Ji, L. Cheng, Y. Liu, L. Nie, Direct measurement of gaseous sodium in flue gas for high-alkali coal, Energy Fuel 33 (2019) 4169–4176.
[50] D.A. Knopf, U. Pöschl, M. Shiraiwa, Radial diffusion and penetration of gas molecules and aerosol particles through laminar flow reactors, denuders, and sampling tubes, Anal. Chem. 87 (2015) 3746–3754.
[51] E. Essuman, G. Meier, J. Żurek, M. Hänsel, W. Quadakkers, The effect of water vapor on selective oxidation of Fe–Cr alloys, Oxid. Met. 69 (2008) 143–162.
[52] E. Essuman, G.H. Meier, J. Żurek, M. Hänsel, L. Singheiser, W.J. Quadakkers, Enhanced internal oxidation as trigger for breakaway oxidation of Fe–Cr alloys in gases containing water vapor, Scr. Mater. 57 (2007) 845–848.
[53] T. Jonsson, S. Karlsson, H. Hooshyar, M. Sattari, J. Liske, J.E. Svensson, L. G. Johansson, Oxidation after breakdown of the chromium-rich scale on stainless steels at high temperature: internal oxidation, Oxid. Met. 85 (2016) 509–536.
[54] N.K. Othman, J. Zhang, D.J. Young, Water vapour effects on Fe–Cr alloy oxidation, Oxid. Met. 73 (2010) 337–352.
[55] H. Yin, S.L.I. Chan, W.Y.D. Yuen, D.J. Young, Temperature effects on the oxidation of low carbon steel in N2–H2–H2O at 800–1200 °C, Oxid. Met. 77 (2012) 305–323.
[56] J. Sui, J. Lehmusto, M. Bergelin, L. Hupa, Initial oxidation mechanisms of stainless steel Sanicro 28 (35Fe27Cr31Ni) exposed to KCl, NaCl, and K2CO3 under dry and humid conditions at 535 °C, Corros. Sci. 155 (2019) 29–45.